

Magnetic reversal in rare-earth free $Mn_4 - xNi_xN$ epitaxial films below and above Ni composition needed for magnetic compensation around room temperature

Cite as: J. Appl. Phys. **127**, 043903 (2020); <https://doi.org/10.1063/1.5128635>

Submitted: 20 September 2019 . Accepted: 05 January 2020 . Published Online: 23 January 2020

Taro Komori, Taku Hirose, Toshiki Gushi, Kaoru Toko, Takayasu Hanashima, Laurent Vila, Jean-Philippe Attané, Kenta Amemiya, and Takashi Suemasu 



View Online



Export Citation



CrossMark

ARTICLES YOU MAY BE INTERESTED IN

[Magnetic and magneto-transport properties of \$Mn_4N\$ thin films by Ni substitution and their possibility of magnetic compensation](#)

Journal of Applied Physics **125**, 213902 (2019); <https://doi.org/10.1063/1.5089869>

[Spin pumping from permalloy into uncompensated antiferromagnetic Co doped zinc oxide](#)

Journal of Applied Physics **127**, 043901 (2020); <https://doi.org/10.1063/1.5131719>

[Strong correlation between uniaxial magnetic anisotropic constant and in-plane tensile strain in \$Mn_4N\$ epitaxial films](#)

AIP Advances **10**, 025117 (2020); <https://doi.org/10.1063/1.5141818>



Your Qubits. Measured.

Meet the next generation of quantum analyzers

- Readout for up to 64 qubits
- Operation at up to 8.5 GHz, mixer-calibration-free
- Signal optimization with minimal latency

Find out more



Magnetic reversal in rare-earth free $\text{Mn}_{4-x}\text{Ni}_x\text{N}$ epitaxial films below and above Ni composition needed for magnetic compensation around room temperature

Cite as: J. Appl. Phys. 127, 043903 (2020); doi: 10.1063/1.5128635

Submitted: 20 September 2019 · Accepted: 5 January 2020 ·

Published Online: 23 January 2020



View Online



Export Citation



CrossMark

Taro Komori,¹ Taku Hirose,¹ Toshiki Gushi,^{1,2} Kaoru Toko,¹ Takayasu Hanashima,³ Laurent Vila,² Jean-Philippe Attané,² Kenta Amemiya,⁴ and Takashi Suemasu^{1,a)} 

AFFILIATIONS

¹Institute of Applied Physics, Graduate School of Pure and Applied Sciences, University of Tsukuba, Tsukuba, Ibaraki 305-8573, Japan

²Université Grenoble Alpes, CEA, CNRS, Spintec, 38000 Grenoble, France

³Neutron Science and Technology Center, CROSS, 162-1 Shirakata, Tokai, Ibaraki 319-1106, Japan

⁴Institute of Materials Structure Science, KEK, Tsukuba 305-0801, Japan

^{a)}Author to whom correspondence should be addressed: suemasu@bk.tsukuba.ac.jp

ABSTRACT

Ferrimagnets close to the magnetic compensation are excellent candidates to spin-torque-based spintronic applications, as their small magnetizations allow lowering switching currents. Here, we studied the magnetic compensation of $\text{Mn}_{4-x}\text{Ni}_x\text{N}$ epitaxial films by performing x-ray absorption spectroscopy (XAS) and x-ray magnetic circular dichroism (XMCD) measurements at the $L_{2,3}$ absorption edges of Mn and Ni atoms and compared them with those of Ni_3FeN films. The XAS spectrum of the Ni_3FeN films exhibits shoulders at approximately 2 eV above the Ni $L_{2,3}$ main peaks, originating from orbitals hybridization between Ni $3d$ at face-centered (II) sites and N $2p$ at body-centered sites. However, such shoulders are not observed at the Ni $L_{2,3}$ edges of the $\text{Mn}_{4-x}\text{Ni}_x\text{N}$ films ($x = 0.1$ and 0.25). These results indicate that the orbitals of Ni atoms do not hybridize with those of N atoms. Hence, Ni atoms preferentially occupy corner (I) sites, where hybridization is weak because of the relatively long distance between Ni at I sites and N atoms. The XMCD signals of Mn and Ni atoms reverse sign between $x = 0.1$ and 0.25 . This shows that the directions of the magnetic moments carried by Mn and Ni atoms are reversed, indicating that the magnetic compensation occurs in the range $0.1 < x < 0.25$. In addition, the signs of Mn(I) XMCD signals are opposite to those of Mn(II) and Ni for each composition. Thus, the magnetic moments of Ni atoms are aligned parallel to those of Mn(II) regardless of whether x is below or above the compensation point.

Published under license by AIP Publishing. <https://doi.org/10.1063/1.5128635>

I. INTRODUCTION

Ferrimagnets are widely researched for their application to spintronics devices.^{1–12} Their key feature is that the magnetic moments of their sublattices are aligned antiparallel to each other. Therefore, some ferrimagnets have a magnetic (and/or angular momentum) compensation point at which the net magnetization (and/or angular momentum) becomes zero, even below the Curie temperature. Spin-transfer torques (STTs) and spin-orbit torques (SOTs) basically consist of a flux of angular momentum carried by an incoming spin current and absorbed by the magnetization. If

the ferrimagnet is at the vicinity of the angular momentum compensation point, the switching is eased and the critical current densities decrease. This can be applied to current-induced domain wall motion (CIDWM) assisted by STTs and SOTs, to create non-volatile memories with high mobility and low power consumption.^{3,4,6,9,10} Theoretically, the spin drift velocity \mathbf{u} induced by the spin-polarized current is given by

$$\mathbf{u} = \frac{Pg\mu_B}{2eM_S} \mathbf{J}, \quad (1)$$

where P is the spin polarization of the electrical conductivity, g is the g -factor, μ_B is the Bohr magneton, e is the elementary charge, M_S is the spontaneous magnetization, and \mathbf{J} is the current density vector.¹³ When $|\mathbf{J}|$ is high enough, we can approximate the domain wall velocity v_{DW} as $|\mathbf{u}|$. Thus, smaller M_S leads to faster v_{DW} . Especially in ferrimagnets, using the definition of g , Eq. (1) can be rewritten as

$$|\mathbf{u}| = \left| \frac{g\mu_B P}{2eM_S} \mathbf{j} \right| = \frac{\hbar}{2e} \left| \frac{P}{M_S^a - M_S^b} \right| \left| \frac{M_S^a - M_S^b}{S^a - S^b} \mathbf{j} \right| = \frac{\hbar}{2e} \left| \frac{Pj}{S^a - S^b} \right|, \quad (2)$$

where S is the spin angular momentum, \hbar is the reduced Planck constant, and superscripts a and b indicate the sublattices of the ferrimagnet. In this way, $|\mathbf{u}|$ ($\approx v_{DW}$) diverges at the angular momentum compensation point ($S^a = S^b$). In experiments, for example, $\text{Gd}_{44}\text{Co}_{56}$ ferrimagnetic nanowires have achieved a v_{DW} of 1.3 km/s assisted by both STT and SOT at 260 K, its angular momentum compensation temperature.⁶ Thus far, many studies have been done on ferrimagnets consisting of both transition-metal (TM) and rare-earth (RE) elements. This is because the temperature dependences of their magnetizations and g -factors are largely different, and thus the angular momentum is easily compensated by tuning temperature and composition.^{2,4,5,11,12} However, RE elements are critical for environmental and geopolitical reasons and are thus expensive and difficult to use on a large scale. In this context, magnetic materials consisting of RE-free elements have attracted attention in this field. Among them, Mn is of particular interest because of the remarkable properties observed in its related compounds. For example, MnAl alloys were reported to have a moderate magnitude of magnetization and high anisotropy, and show a large maximum energy product of about 100 kJ/m³.¹⁴ α -MnBi was also reported to show a large perpendicular magnetic anisotropy (PMA) at room temperature (RT), and studies on exchange interaction between MnBi and FeCo thin films have been carried out to realize a PMA material with large magnetization.^{15,16} Furthermore, artificial ferrimagnet-like PMA materials were achieved using MnGa/Co₂MnSi multilayers, and the magnetic compensation (MC) was confirmed by controlling layer thickness and temperature.¹⁵ Despite these progresses, however, RE-free ferrimagnet with a compensation point close to RT has not been reported.

Here, we propose to focus on $\text{Mn}_{4-x}\text{Ni}_x\text{N}$ films, showing, in particular, that for the right Ni concentration this RE-free ferrimagnet can reach the angular compensation at RT. These films are related to Mn_4N films, a new RE-free ferrimagnetic material.^{17–25} Figure 1 shows the crystal structure and direction of magnetic moments of Mn atoms in the Mn_4N lattice. We label the corner and face-centered atomic sites as I and II, respectively. The II sites are further divided into IIA and IIB sites in the presence of magnetization (arrow in Fig. 1). N atoms are at the body-centered sites. Neutron diffraction measurement shows the magnetic moments of the Mn atoms in bulk Mn_4N to be $3.53\mu_B$ at I sites and $-0.89\mu_B$ at II sites with the easy magnetization axis along the [111] direction.^{26,27} However, Mn_4N films have PMA with a magnetic anisotropy constant K_u of approximately 10^5 J/m^3 .^{18–22,24,25} Materials with PMA generally form Bloch walls, leading to faster domain wall motion with low current density.^{13,28} Furthermore, the spontaneous magnetization M_S of

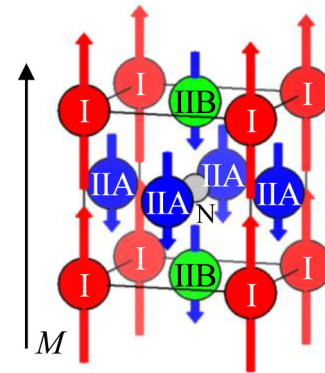


FIG. 1. Crystalline structure of antiperovskite-type Mn_4N and magnetic moments of Mn atoms. Face-centered sites (II) can be further divided into IIA and IIB sites with magnetization.

$\text{Mn}_{4-x}\text{Ni}_x\text{N}$ films is approximately 100 kA/m, which is relatively small compared to those of other magnetic materials.^{21,22,24,25} Gushi *et al.* achieved a v_{DW} of approximately 900 m/s with a current density of $1.2 \times 10^{12} \text{ A/m}^2$ at RT,¹⁹ which is a record v_{DW} for CIDWM only by STT. Although the compensation temperature of Mn_4N has not been reported, Mekata found that magnetic compensation (MC) occurred in Mn_4N at RT when a proper amount of Mn was substituted with In or Sn atoms.²⁹ On this basis, mixed crystal nitride films derived from Mn_4N are expected to have both PMA with low M_S and a compensation point, leading to more efficient domain wall motion. We have succeeded in fabricating such nitrides as $\text{Fe}_{4-x}\text{Mn}_x\text{N}$,²² $\text{Mn}_{4-x}\text{Co}_x\text{N}$,²³ and $\text{Mn}_{4-x}\text{Ni}_x\text{N}$ ^{24,25} epitaxial films. Compared with Mn_4N , $\text{Mn}_{4-x}\text{Ni}_x\text{N}$ films have shown an anomalous decrease in M_S of 45% at $x=0.1$ and 75% at $x=0.25$, while the PMA is preserved. We further concluded that $\text{Mn}_{4-x}\text{Ni}_x\text{N}$ films have a MC composition at RT because the signs of the anomalous Hall resistivity and M_S temperature dependences were different between $x=0.1$ and 0.25 .²⁵ The latter two trends were also similar to those of $\text{Mn}_{4-x}\text{In}_x\text{N}$ and $\text{Mn}_{4-x}\text{Sn}_x\text{N}$, in which Mekata demonstrated the existence of a MC.²⁹ However, the magnetic structures and preferential occupation sites of Ni atoms in $\text{Mn}_{4-x}\text{Ni}_x\text{N}$ are not yet known.

X-ray absorption spectroscopy (XAS) and x-ray magnetic circular dichroism (XMCD) are powerful techniques for determining element-specific electronic structures. We have performed these measurements on Fe_4N ,³⁰ Co_4N ,³¹ $\text{Co}_x\text{Fe}_{4-x}\text{N}$,^{31,32} and $\text{Ni}_x\text{Fe}_{4-x}\text{N}$ ³³ epitaxial films, all of which are antiperovskite ferromagnetic nitrides. In the XAS spectra of Fe_4N and Co_4N , shoulders above the $L_{2,3}$ absorption edges have appeared approximately 2 eV above the main peaks, and they have been explained by the orbital hybridization between $3d$ orbitals of face-centered Fe(II) or Co(II) atoms and $2p$ orbitals of body-centered N atoms.^{30,31} The same phenomenon has been observed for the other nitrides mentioned above. Takata *et al.* successfully determined the preferential occupation site of Ni atoms in $\text{Ni}_x\text{Fe}_{4-x}\text{N}$ ($x=1$ and 3) from the presence and absence of shoulders in the Ni $L_{2,3}$ XAS spectra for each composition.³³ In this work, we performed XAS and XMCD measurements on $\text{Mn}_{4-x}\text{Ni}_x\text{N}$ ($x=0.1$ and 0.25) epitaxial films and found the preferential occupation site of Ni atoms in

$\text{Mn}_{4-x}\text{Ni}_x\text{N}$ to be I sites. Using the obtained results, we propose a model describing the magnetic moments of Ni and Mn atoms below and above the Ni MC composition in $\text{Mn}_{4-x}\text{Ni}_x\text{N}$ films.

II. EXPERIMENTAL

10-nm-thick $\text{Mn}_{4-x}\text{Ni}_x\text{N}$ ($x=0.1$ and 0.25) epitaxial films have been grown on SrTiO_3 [STO](001) substrates using molecular beam epitaxy, using high-temperature Knudsen cells with solid Mn and Ni sources and a radio-frequency N plasma source. The substrate temperature was set at 450°C during growth. The growth procedure is detailed in Ref. 25. After growth, the samples were capped *in situ* with Ti to prevent oxidation. The crystalline quality of the grown films was characterized via reflection high-energy electron diffraction (RHEED) and out-of-plane ($\omega-2\theta$) and in-plane ($\phi-2\theta\chi$) x-ray diffraction (XRD). The polar Kerr effect was measured with a magneto-optical Kerr effect (MOKE) microscope to determine whether each sample composition was below or above the MC level, by looking at the sign of the measured hysteresis loops. The magnetic field μ_0H was applied perpendicularly to the plane in the range $\mu_0H = -1.25$ – 1.25 T. The same method was used in Ref. 6. XAS and XMCD measurements were performed at the twin APPLE-II undulator beam line BL-16A of KEK in Japan.³⁴ Both a magnetic field of ± 3 T and circularly polarized x rays with left or right polarization were applied perpendicularly to the plane. The x-ray polarization was switched at every energy point with a frequency of 10 Hz using five kicker magnets. Spectra were acquired at RT in total electron yield mode and total fluorescence yield mode at the Mn $L_{2,3}$ and Ni $L_{2,3}$ absorption edges, respectively, in order to prevent Ni $L_{2,3}$ spectra from overlapping with background signals.

III. RESULTS AND DISCUSSION

Figure 2 shows the XRD results and RHEED images taken along the [100] azimuth of STO(001) after the growth of the $\text{Mn}_{4-x}\text{Ni}_x\text{N}$ films. Because of the excellent lattice matching between $\text{Mn}_{4-x}\text{Ni}_x\text{N}$ and STO(001), the diffraction peaks of the STO substrate overlap with those of the $\text{Mn}_{4-x}\text{Ni}_x\text{N}$ films. The $\text{Mn}_{4-x}\text{Ni}_x\text{N}$ peaks still appear at a slightly larger angle 2θ than those of the cubic STO in the $\omega-2\theta$ XRD pattern of Figs. 2(a)–2(d), while they are missing from the $\phi-2\theta\chi$ XRD in Figs. 2(e) and 2(f). In Figs. 2(c) and 2(d), we recognize the presence of 002 peaks and satellite peaks. We can also see a clear Laue fringe in the RHEED patterns. These results highlight the formation of high-quality epitaxial films. Assuming that STO has a perfect cubic structure, the lattice constants determined for $\text{Mn}_{4-x}\text{Ni}_x\text{N}$ have the relation $c < a$, suggesting the presence of an in-plane tensile strain. This was also found in our previous work on Mn_4N and $\text{Mn}_{4-x}\text{Ni}_x\text{N}$ films.^{24,25} The sharp diffraction peaks of $\text{Mn}_{4-x}\text{Ni}_x\text{N}$ 004 with fine streaky patterns and the Kikuchi lines in the RHEED images suggest that the grown films are epitaxial and highly c -axis-oriented. We ascribe the lines indicated by white arrows in the RHEED images to superlattice diffraction, with N atoms correctly located at the lattice center. Furthermore, a diffraction peak at around $2\theta = 41^\circ$ – 42° is found in each $\phi-2\theta\chi$ XRD pattern. We ascribe this peak to Mn-related oxides.²⁵

Figure 3 shows the polar MOKE hysteresis loops of $\text{Mn}_{3.9}\text{Ni}_{0.1}\text{N}$ ($x=0.1$) (a) and $\text{Mn}_{3.75}\text{Ni}_{0.25}\text{N}$ ($x=0.25$) (b) films at

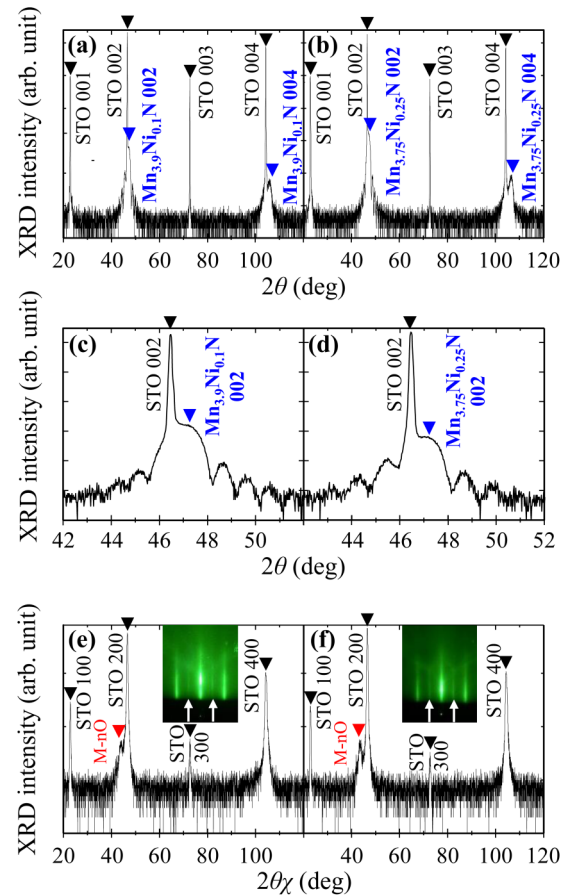


FIG. 2. XRD profiles of $\text{Mn}_{3.9}\text{Ni}_{0.1}\text{N}$ films [(a), (c), (e)] and $\text{Mn}_{3.75}\text{Ni}_{0.25}\text{N}$ [(b), (d), (f)] films on STO(001). (a) and (b) Out-of-plane XRD patterns and [(c) and (d)] their enlarged figures at around $2\theta = 46^\circ$. (e) and (f) In-plane XRD patterns. The insets show the RHEED images of the $\text{Mn}_{3.9}\text{Ni}_{0.1}\text{N}$ and $\text{Mn}_{3.75}\text{Ni}_{0.25}\text{N}$ films taken along the STO[100] azimuth. Lines marked by white arrows suggest superlattice diffraction.

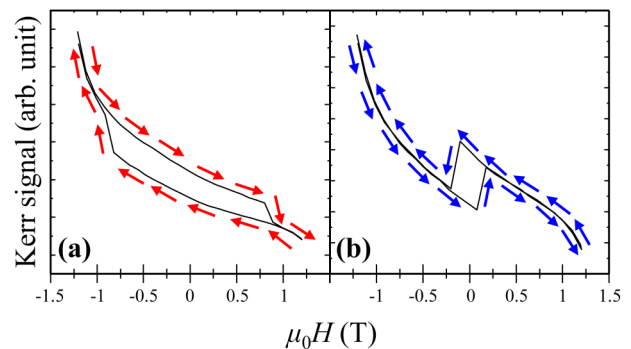


FIG. 3. Polar MOKE hysteresis loops of (a) $\text{Mn}_{3.9}\text{Ni}_{0.1}\text{N}$ and (b) $\text{Mn}_{3.75}\text{Ni}_{0.25}\text{N}$ films. The magnetic field was scanned as marked by arrows. Note the reversal of the hysteresis loops.

RT. The distortion of the loops at high magnetic field regions was caused by non-linear Faraday rotations of the polarized light that occur in the objective lens.³⁵ When the external magnetic field exceeded the coercivity, the magnetization reversed, and thus the MOKE image reversed. This behavior is different between $x=0.1$ and 0.25 as shown by the arrows, indicating the presence of a Ni composition corresponding to the magnetic compensation between them. A similar result was reported in ferrimagnets CoGd and Co/Ti/(Gd-Co) multilayers near the compensation of magnetization and angular momentum.^{11,36} The sharp corners of the loop, very similar to what has been observed in $\text{Mn}_4\text{N}/\text{STO}(001)$,¹⁹ are a hint of the quality of the magnetic properties, with a smooth magnetization reversal by domain wall (DW) propagation. We ascribe this result to the excellent lattice matching between $\text{STO}(001)$ and $\text{Mn}_{4-x}\text{Ni}_x\text{N}$.¹⁴ Note that $\text{Mn}_{3.9}\text{Ni}_{0.1}\text{N}$ shows a higher coercivity than $\text{Mn}_{3.75}\text{Ni}_{0.25}\text{N}$ and than the sample with the same composition fabricated in our previous work.²⁵ This is probably due to the fact that the composition of the sample fabricated in this work is closer to the compensation composition.^{11,36} The composition ratio of Mn and Ni is calculated only via their deposition rate ratios from the Knudsen cells in this work.

Figures 4(a) and 4(b) show the XAS and XMCD spectra of $\text{Mn}_{3.9}\text{Ni}_{0.1}\text{N}$ and $\text{Mn}_{3.75}\text{Ni}_{0.25}\text{N}$ films at the Ni $L_{2,3}$ absorption edges, respectively. We compare these spectra with those reported for Ni_3FeN in Fig. 4(c) and NiFe_3N in Fig. 4(d).³³ Regarding the XAS spectra of $\text{Mn}_{3.9}\text{Ni}_{0.1}\text{N}$ and $\text{Mn}_{3.75}\text{Ni}_{0.25}\text{N}$ films, only the sharp main peaks are observed at the L_3 edge (852–853 eV) and the L_2 edge (870 eV). In contrast, we see shoulders in the XAS spectrum of Ni_3FeN films marked by arrows in Fig. 4(c). These shoulders are observed approximately 2 eV above the Ni $L_{2,3}$ main peaks. Such shoulders are reported for other antiperovskite ferromagnetic nitrides such as Fe_4N and Co_4N films above the Fe (Co) $L_{2,3}$ main peaks.^{30,31} These are interpreted to originate from the electric dipole transition from the metal $2p$ core level to the hybrid state between the orbitals of the N $2p$ and metal $3d$ at II sites, indicating that the objective element is at II sites.³⁰ However, these shoulders are missing in the XAS spectrum of NiFe_3N films in Fig. 4(d). In $\text{Ni}_x\text{Fe}_{4-x}\text{N}$, the preferential sites of Ni atoms determined by XAS measurements agree well with those obtained via Mössbauer measurements and first-principles calculations based on the configuration-dependent total energy.^{33,37,38} Thus, we have a reasonable confidence in the results obtained for $\text{Mn}_{4-x}\text{Ni}_x\text{N}$ as

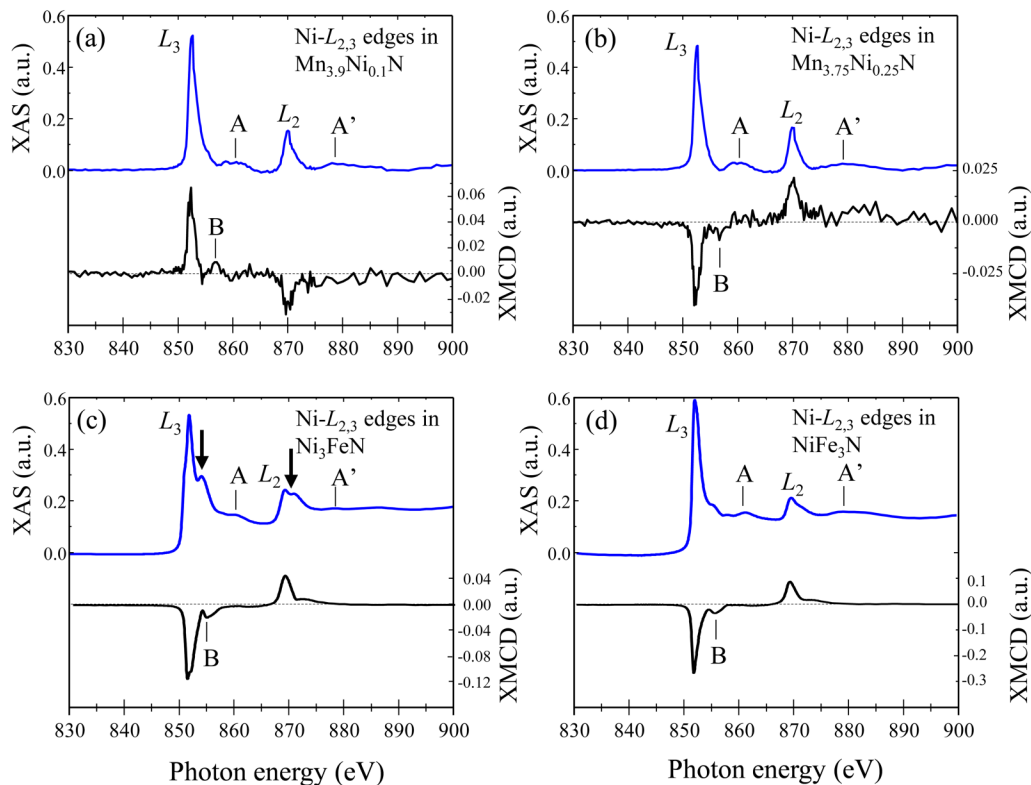


FIG. 4. XAS (blue) and XMCD (black) spectra in (a) $\text{Mn}_{3.9}\text{Ni}_{0.1}\text{N}$ films and (b) $\text{Mn}_{3.75}\text{Ni}_{0.25}\text{N}$ films at Ni $L_{2,3}$ edges. XAS spectra in (c) Ni_3FeN films and (d) NiFe_3N films at Ni $L_{2,3}$ edges.³³ Note the reversal of the XMCD signals between (a) and (b), meaning that the direction of magnetic moment of Ni is flipped between them. The arrows in (c) indicate the presence of Ni at face-centered II sites. Satellites A and A' are reproducible by a one-electron relativistic tight-binding calculation.⁴¹ Satellites B and B' are mainly due to the configuration interaction between the final-state multiples described with $2p^53d^9$ and $2p^53d^{10}$.⁴² Data in (c) and (d) reproduced with permission from Takata *et al.*, Phys. Rev. Mater. 2, 024407 (2018). Copyright 2018 American Physical Society.

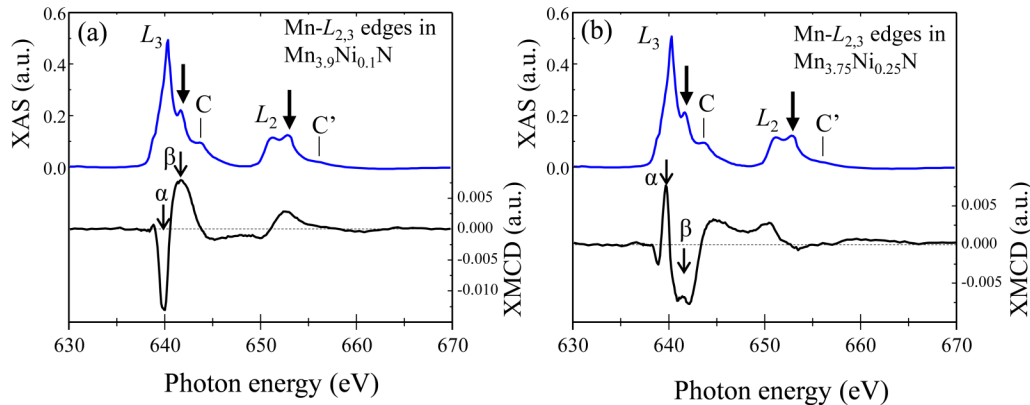


FIG. 5. XAS (blue) and XMCD (black) spectra in (a) $\text{Mn}_{3.9}\text{Ni}_{0.1}\text{N}$ films and (b) $\text{Mn}_{3.75}\text{Ni}_{0.25}\text{N}$ films at Mn $L_{2,3}$ edges. The sharp peak (α) and broad peak (β) originate mainly from Mn(I) and Mn(II), respectively. The different sign of the XMCD signal between them indicates that the magnetic moment of Mn(I) is antiparallel to that of Mn(II). Note the reversal of the XMCD signals between (a) and (b), meaning that the magnetic moment of Mn is flipped between them. Satellites C and C' originate from Mn-related oxides.

well. From these results, we can safely state that Ni atoms preferentially occupy the I sites in Mn_4N when $x \leq 0.25$. In addition to the shoulders mentioned above, Figs. 4(a)–4(d) show other distinct satellites marked as A and A'. Let us now discuss their origins. Satellites A and A' are observed at approximately 7 eV above the Ni L_3 and L_2 edges. We initially considered their origin to be the hybrid state between the Ni $3d$ and O $2p$ orbitals. However, they are reported to be only 1.5 eV above the Ni $L_{2,3}$ edges.³⁹ Thus, this value does not agree with our results in this work. These are rather close to the satellite positions reported for the Ni $L_{2,3}$ edges of $\text{Ni}_x\text{Fe}_{4-x}\text{N}$. Such satellites are also reported for pure fcc-Ni both in experiments and in a one-electron relativistic tight-binding calculation.^{40,41}

The XMCD spectra for Ni are simple. The peak signs are opposite at the $L_{2,3}$ edges between $\text{Mn}_{3.9}\text{Ni}_{0.1}\text{N}$ and $\text{Mn}_{3.75}\text{Ni}_{0.25}\text{N}$. Thus, the directions of magnetic moments of Ni(I) in $\text{Mn}_{3.9}\text{Ni}_{0.1}\text{N}$ films are different from that in $\text{Mn}_{3.75}\text{Ni}_{0.25}\text{N}$ films with respect to the magnetizations. Regarding satellite B in Figs. 4(a)–4(d), it has been found only experimentally, without being reproduced by calculations.⁴² This can be understood by considering that satellite B results from the interaction between the final-state multiples described with $2p^53d^9$ and $2p^53d^{10}$. Although no distinct satellite is observed in the XMCD spectra above the Ni L_2 edges, it has been experimentally confirmed elsewhere.⁴³ We conclude that the satellite intensity is weak owing to the small atomic ratio of Ni and that the satellites are buried in background signals.

We next move on to the XAS and XMCD spectra of $\text{Mn}_{3.9}\text{Ni}_{0.1}\text{N}$ [Fig. 5(a)] and $\text{Mn}_{3.75}\text{Ni}_{0.25}\text{N}$ films [Fig. 5(b)] at the Mn $L_{2,3}$ absorption edges. Shoulders marked by arrows and satellites (C, C') are observed at approximately 2 eV and 3.5 eV, respectively, above the Mn $L_{2,3}$ main peaks of the $\text{Mn}_{3.9}\text{Ni}_{0.1}\text{N}$ and $\text{Mn}_{3.75}\text{Ni}_{0.25}\text{N}$ films. Note that similar features were observed in the XAS spectra of Mn-related oxides such as MnFe_2O_4 ⁴⁴ and are characterized by the final-state multiples of the $2p^53d^6$ configuration from a highly localized Mn^{2+} ground state. As mentioned before,

oxygen atoms may be present in the samples containing the Mn oxide as shown in Figs. 2(e) and 2(f).

The XMCD spectra of these films also show some complexity. The signs of the XMCD signals around the Mn L_3 edge are positive, negative, and positive from low to high photon energy in $\text{Mn}_{3.9}\text{Ni}_{0.1}\text{N}$. The superposition of spectra with different signs indicates that the magnetic moments of Mn(I) and Mn(II) are aligned antiparallel to each other. In our previous studies on Fe_4N films, the transition metals at the I(II) site exhibit localized (itinerant) states supported by the first-principles calculation using the all-electron full-potential linearized augmented-plane-wave (FLAPW) method and Fermi's golden rule with E1 transitions.³⁰ Similar calculation results are also supported for Mn_4N by the FLAPW calculation.⁴⁵

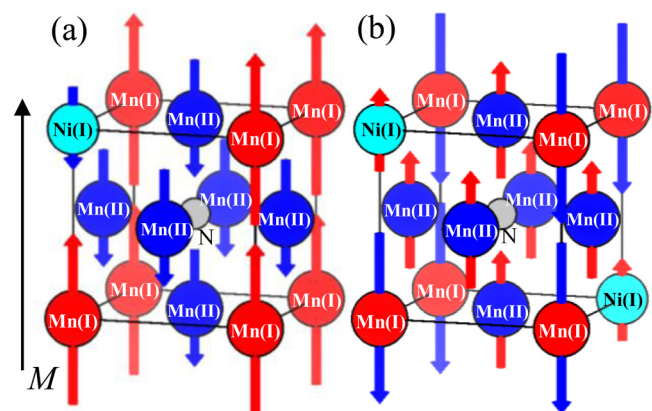


FIG. 6. Schematics of the magnetic structures in $\text{Mn}_{4-x}\text{Ni}_x\text{N}$ [below the MC composition ratio in (a) and above it in (b)]. The magnetic moment of Mn(I) is aligned antiparallel to those of Mn(II) and Ni(I).

TABLE I. Spin (m_{spin}), orbital (m_{orb}), and total (m_{tot}) magnetic moments of Mn and Ni atoms in $\text{Mn}_{4-x}\text{Ni}_x\text{N}$ deduced by sum-rule analysis.

Compounds	Atom	Magnetic moment (μ_B per atom)		
		m_{spin}	m_{orb}	m_{tot}
$\text{Mn}_{3.9}\text{Ni}_{0.1}\text{N}$	Mn	0.024 ± 0.011	-0.016 ± 0.002	0.008 ± 0.014
	Ni	-0.20 ± 0.03	-0.024 ± 0.004	-0.22 ± 0.03
$\text{Mn}_{3.75}\text{Ni}_{0.25}\text{N}$	Mn	0.081 ± 0.020	0.011 ± 0.005	0.092 ± 0.025
	Ni	0.17 ± 0.02	0.010 ± 0.002	0.18 ± 0.02

Therefore, the XMCD spectra of $\text{Mn}_{3.9}\text{Ni}_{0.1}\text{N}$ and $\text{Mn}_{3.75}\text{Ni}_{0.25}\text{N}$ films can also be viewed as an overlap of such localized and itinerant components characterized by features α and β , respectively, with opposite signs. In $\text{Mn}_{3.9}\text{Ni}_{0.1}\text{N}$, the broad positive peak (β) near 642 eV likely originates from Mn(II) atoms because of the hybridization between Mn(II) 3d and N 2p orbitals. In contrast, the sharp negative peak (α) near 640 eV likely comes from Mn(I), which is remote from N, and therefore entails less hybridization. Note that the signs of the XMCD signals near the Mn L_3 absorption edges are negative, positive, and negative from low to high photon energy in $\text{Mn}_{3.75}\text{Ni}_{0.25}\text{N}$, which is the opposite of the results obtained for the $\text{Mn}_{3.9}\text{Ni}_{0.1}\text{N}$ films. We attribute this to magnetization reversal at both I and II sites. Such behavior of the spectra was reported in ferrimagnets at the vicinity of the compensation temperature.^{46,47} It is also notable that the XMCD signal at the Ni L_3 absorption edge has the opposite sign of the sharp peak for the Mn L_3 edge at 640 eV regardless of x and has the same sign as that of the broad spectrum at 642 eV. The former mainly comes from Mn(I) atoms and the latter from Mn(II) atoms. Thus, the magnetic moments of Ni(I) always align in parallel with those of Mn(II) or in antiparallel with those of Mn(I) in the studied range of x .

From these discussions, we conclude that the preferential occupation site of Ni is the I site in $\text{Mn}_{4-x}\text{Ni}_x\text{N}$ thin films and that the magnetic moments of Ni atoms are parallel to those of Mn (II). On the basis of these conclusions, Fig. 6 shows the simplified schematics of the magnetic structures in $\text{Mn}_{4-x}\text{Ni}_x\text{N}$ [below the MC composition ratio in (a) and above it in (b)]. Here, we assumed that all Ni atoms occupy I sites, which we believe is reasonable from Fig. 4 and the above discussions. We used the $x = 0.1$ and 0.25 samples in the experiment; however, the composition ratios are 0.125 for Fig. 6(a) and 0.25 for Fig. 6(b) to simplify the representation. As mentioned in Fig. 1, Mn_4N is a ferrimagnetic material in which the magnetic moments of the Mn(I) atoms are aligned parallel to the magnetic field H and antiparallel to the moments of the Mn(II) atoms. The magnetic moments of the Mn (I) sites thus determine the direction of M_S . For $x = 0.1$, some Mn (I) atoms are replaced with Ni atoms, and the magnetic moments of the Ni(I) atoms are parallel to those of Mn(II). This results in a net decrease in M_S ,²¹ and the Mn(I) atoms still determine the direction of M_S . When x is increased further to 0.25, more Mn(I) atoms are replaced with Ni atoms to the extent where the sum of the magnetic moments aligned antiparallel to magnetic field becomes greater than that of those aligned parallel to it. In this state, the net magnetization and magnetic field are antiparallel,

causing an unstable Zeeman energy state. Thus, all magnetic moments need to flip to achieve the stable state shown in Fig. 6(b). As a result, the magnetic moments of the Mn(II) sites determine the direction of M_S at $x = 0.25$. Therefore, we can safely state that the MC occurs at a value of x between 0.1 and 0.25.

We finally discussed the spin (m_{spin}), orbital (m_{orb}), and total ($m_{\text{tot}} = m_{\text{spin}} + m_{\text{orb}}$) magnetic moments per Mn and Ni atom for the samples at $x = 0.1$ and 0.25 deduced by applying the sum-rule analysis.^{48,49} We subtracted the background signals of the XAS spectra by a two-step function aligned at the peak maxima of the L_3 and L_2 edges. As the hole numbers (n_h) of Mn and Ni atoms, we adopted 5.2 for Mn⁵⁰ regardless of I and II sites and 1.4 for Ni.^{51,52} The same assumption was made in a previous study on $\text{Fe}_{4-x}\text{Ni}_x\text{N}$,⁵³ wherein the n_h of the two different sites has been reported to be almost the same by the first-principles calculation. The obtained m_{spin} , m_{orb} , and m_{tot} are summarized in Table I. The sign of the magnetic moment of Ni atoms was negative at $x = 0.1$, meaning that the magnetic moment of Ni atoms aligns in antiparallel with the magnetization. In contrast, the sign reversed at $x = 0.25$. We also notice that the magnitude of m_{tot} for Ni atoms remained almost unchanged between $x = 0.1$ and 0.25, suggesting that the preferential occupation site of Ni atoms did not change. These results are consistent with the above discussions based on the XMCD spectra. The m_{tot} per unit cell was calculated to be approximately $0.009\mu_B$ for $x = 0.1$ and $0.39\mu_B$ for $x = 0.25$, corresponding to approximately 1.5 kA/m and 63 kA/m, respectively. Note that m_{tot} at $x = 0.1$ is very small. As previously mentioned about the higher coercivity in the MOKE hysteresis loop at $x = 0.1$ in Fig. 3(a), we can state that the Ni composition $x = 0.1$ is really close to the compensation composition.

IV. CONCLUSION

We performed XAS and XMCD measurements at the Mn and Ni $L_{2,3}$ absorption edges of $\text{Mn}_{4-x}\text{Ni}_x\text{N}$ epitaxial films for $x = 0.1$ and 0.25. Although shoulders were observed at photon energies of approximately 2 eV above the main peaks of the Mn $L_{2,3}$ edges, no such features were observed for Ni atoms. We attribute these shoulders to orbital hybridization between Mn(II) atoms at face-centered sites and N atoms at body-centered sites and therefore conclude that the Ni atoms preferentially occupy I sites at least at $x \leq 0.25$. Spectral line-shape analysis revealed that the magnetic moments of Mn(II) atoms were aligned parallel to those of Ni atoms and antiparallel to those of Mn(I) atoms and to H at $x = 0.1$. However, all the magnetic moments of these atoms are reversed at $x = 0.25$, and

the magnetic moments of Mn(II) atoms were aligned parallel to H . These results mean that the magnetic moments of Mn(I) atoms determine the direction of M_S at $x = 0.1$, while those of Mn(II) determine it at $x = 0.25$. The m_{spin} and m_{orb} values were deduced from the obtained XAS and XMCD spectra by sum-rule analysis, and the sign reversal of the magnetic moment of Ni atoms between 0.1 and 0.25 was confirmed. These results show that the MC composition x for Ni in $\text{Mn}_{4-x}\text{Ni}_x\text{N}$ is between 0.1 and 0.25. We thus believe that with the absence of RE elements, and with the possibility to obtain angular magnetic compensation at room temperature, $\text{Mn}_{4-x}\text{Ni}_x\text{N}$ is a very attractive candidate for applications based on STT or SOT.

ACKNOWLEDGMENTS

This work was supported by Grants-in-Aid for Scientific Research from the Japan Society for the Promotion of Science (Nos. 19K04499, 19K21954, and 19KK0104). The XMCD experiment was performed at beam line BL-16A of KEK-PF with the approval of the Photon Factory Program Advisory Committee (Proposal No. 2018P011). The Kerr rotation measurement was done with the help of Dr. S. Mitani of the National Institute for Materials Science, Tsukuba, Japan.

REFERENCES

- ¹C. D. Stanciu, A. V. Kimel, F. Hansteen, A. Tsukamoto, A. Itoh, A. Kirilyuk, and T. Rasing, *Phys. Rev. B* **73**, 220402(R) (2006).
- ²C. D. Stanciu, A. Tsukamoto, A. V. Kimel, F. Hansteen, A. Kirilyuk, A. Itoh, and T. Rasing, *Phys. Rev. Lett.* **99**, 217204 (2007).
- ³S. Fukami, T. Suzuki, Y. Nakatani, N. Ishiwata, M. Yamanouchi, S. Ikeda, N. Kasai, and H. Ohno, *Appl. Phys. Lett.* **98**, 082504 (2011).
- ⁴K.-J. Kim, S. K. Won, Y. Hirata, S.-H. Oh, T. Tono, D.-H. Kim, T. Okuno, W. S. Ham, S. Kim, G. Go, Y. Tserkovnyak, A. Tsukamoto, T. Moriyama, K.-J. Lee, and T. Ono, *Nat. Mater.* **16**, 1187 (2017).
- ⁵Y. Hirata, D.-H. Kim, T. Okuno, T. Nishimura, D.-Y. Kim, Y. Futakawa, H. Yoshikawa, A. Tsukamoto, K.-J. Kim, S.-B. Choe, and T. Ono, *Phys. Rev. B* **97**, 220403(R) (2018).
- ⁶L. Caretta, M. Mann, F. Buttner, K. Ueda, B. Pfau, C. M. Gunther, P. Helsing, A. Churikova, C. Klose, M. Schneider, D. Engel, C. Marcus, D. Bono, K. Bagschik, S. Eisebitt, and G. S. D. Beach, *Nat. Nanotechnol.* **13**, 1154 (2018).
- ⁷S. A. Siddiqui, J. Han, J. T. Finley, C. A. Ross, and L. Liu, *Phys. Rev. Lett.* **121**, 057701 (2018).
- ⁸S.-H. Oh, S. K. Kim, D.-K. Lee, G. Go, K.-J. Kim, T. Ono, Y. Tserkovnyak, and K.-J. Lee, *Phys. Rev. B* **96**, 100407(R) (2017).
- ⁹R. Blasing, T. Ma, S.-H. Yang, C. Garg, F. K. Dejene, A. T. N'Diaye, G. Chen, K. Liu, and S. S. P. Parkin, *Nat. Commun.* **9**, 4984 (2018).
- ¹⁰S.-H. Yang, K.-S. Ryu, and S. Parkin, *Nat. Nanotechnol.* **10**, 221 (2015).
- ¹¹M. Binder, A. Weber, O. Mosendz, G. Woltersdorf, M. Izquierdo, I. Neudecker, J. R. Dahn, T. D. Hatchard, J.-U. Thiele, C. H. Back, and M. R. Scheinfein, *Phys. Rev. B* **74**, 134404 (2006).
- ¹²T. Okuno, K.-J. Kim, T. Tono, S. Kim, T. Moriyama, H. Yoshikawa, A. Tsukamoto, and T. Ono, *Appl. Phys. Express* **9**, 073001 (2016).
- ¹³A. Thiaville, Y. Nakatani, J. Miltat, and Y. Suzuki, *Europhys. Lett.* **69**, 990 (2005).
- ¹⁴J. Cui, M. Kramer, L. Zhou, F. Liu, A. Gabay, G. Hadjipanayis, B. Balasubramanian, and D. Sellmyer, *Acta Mater.* **158**, 118 (2018).
- ¹⁵S. Sabet, A. Moradabadi, S. Gorji, M. Yi, Q. Gong, M. H. Fawey, E. Hildebrandt, D. Wang, H. Zhang, B.-X. Xu, C. Kübel, and L. Alff, *Phys. Rev. B* **98**, 174440 (2018).
- ¹⁶J. Lu, S. Mao, X. Zhao, X. Wang, J. Liu, J. Xia, P. Xiong, and J. Zhao, *Sci. Rep.* **7**, 16990 (2017).
- ¹⁷Y. Yasutomi, K. Ito, T. Sanai, K. Toko, and T. Suemasu, *J. Appl. Phys.* **115**, 17A935 (2014). 4
- ¹⁸T. Gushi, L. Vila, O. Fruchart, A. Marty, S. Pizzini, J. Vogel, F. Takata, A. Anzai, K. Toko, T. Suemasu, and J.-P. Attané, *Jpn. J. Appl. Phys.* **57**, 120310 (2018).
- ¹⁹T. Gushi, M. J. Klug, J. P. Garcia, S. Ghosh, J. P. Attané, H. Okuno, O. Fruchart, J. Vogel, T. Suemasu, S. Pizzini, and L. Vila, *Nano Lett.* **19**, 8716 (2019).
- ²⁰X. Shen, A. Chikamatsu, K. Shigematsu, Y. Hirose, T. Fukumura, and T. Hasegawa, *Appl. Phys. Lett.* **105**, 072410 (2014).
- ²¹K. Kabara and M. Tsunoda, *J. Appl. Phys.* **117**, 17B512 (2015).
- ²²A. Anzai, F. Takata, T. Gushi, K. Toko, and T. Suemasu, *J. Cryst. Growth* **489**, 20 (2018).
- ²³K. Ito, Y. Yasutomi, K. Kabara, T. Gushi, S. Higashikozono, K. Toko, M. Tsunoda, and T. Suemasu, *AIP Adv.* **6**, 056201 (2016).
- ²⁴T. Komori, A. Anzai, T. Gushi, K. Toko, and T. Suemasu, *J. Cryst. Growth* **507**, 163 (2019).
- ²⁵T. Komori, T. Gushi, A. Anzai, L. Vila, J.-P. Attané, S. Pizzini, J. Vogel, S. Isogami, K. Toko, and T. Suemasu, *J. Appl. Phys.* **125**, 213902 (2019).
- ²⁶W. J. Takei, R. R. Heikes, and G. Shirane, *Phys. Rev. B* **125**, 1893 (1962).
- ²⁷C. Li, Y. Yang, L. Lv, H. Huang, Z. Wang, and S. Yang, *J. Alloys Compd.* **457**, 57 (2008).
- ²⁸S. Emori and G. S. D. Beach, *Appl. Phys. Lett.* **98**, 132508 (2011).
- ²⁹M. Mekata, *J. Phys. Soc. Jpn.* **17**, 5 (1962).
- ³⁰K. Ito, K. Toko, Y. Takeda, Y. Saitoh, T. Oguchi, T. Suemasu, and A. Kimura, *J. Appl. Phys.* **117**, 193906 (2015).
- ³¹K. Ito, T. Sanai, Y. Yasutomi, S. Zhu, K. Toko, Y. Takeda, Y. Saitoh, A. Kimura, and T. Suemasu, *J. Appl. Phys.* **115**, 17C712 (2014).
- ³²K. Ito, T. Sanai, S. Zhu, Y. Yasutomi, K. Toko, S. Honda, S. Ueda, Y. Takeda, Y. Saitoh, Y. Imai, A. Kimura, and T. Suemasu, *Appl. Phys. Lett.* **103**, 232403 (2013).
- ³³F. Takata, K. Ito, Y. Takeda, Y. Saitoh, K. Takashi, A. Kimura, and T. Suemasu, *Phys. Rev. Mater.* **2**, 024407 (2018).
- ³⁴K. Amemiya, M. Sakamaki, T. Koide, K. Ito, K. Tsuchiya, K. Harada, T. Aoto, T. Shioya, T. Obina, S. Yamamoto, and Y. Kobayashi, *J. Phys.: Conf. Ser.* **425**, 152015 (2013).
- ³⁵I. V. Soldatov and R. Schäfer, *J. Appl. Phys.* **122**, 153906 (2017).
- ³⁶A. V. Svalov, A. Fernandez, V. O. Vas'kovskiy, G. V. Kurlyandskaya, J. M. Banrandiarán, R. L. Anton, and M. Tejedor, *J. Alloys Compd.* **419**, 25 (2006).
- ³⁷F. Li, J. Yang, D. Xue, and R. Zhou, *Appl. Phys. Lett.* **66**, 2343 (1995).
- ³⁸P. Monachesi, T. Björkman, T. Gasche, and O. Eriksson, *Phys. Rev. B* **88**, 054420 (2013).
- ³⁹D. Alders, F. C. Voogt, T. Hibma, and G. A. Sawatzky, *Phys. Rev. B* **54**, 7716 (1996).
- ⁴⁰C. T. Chen, F. Sette, Y. Ma, and S. Modesti, *Phys. Rev. B* **42**, 7262 (1990).
- ⁴¹K. Amemiya, E. Sakai, D. Matsumura, H. Abe, and T. Ohta, *Phys. Rev. B* **72**, 201404(R) (2005).
- ⁴²N. V. Smith, C. T. Chen, F. Sette, and L. F. Mattheiss, *Phys. Rev. B* **46**, 1023 (1992).
- ⁴³T. Jo and G. A. Sawatzky, *Phys. Rev. B* **43**, 8771 (1991).
- ⁴⁴J.-S. Kang, G. Kim, H. J. Lee, D. H. Kim, H. S. Kim, J. H. Shim, S. Lee, H. Lee, J.-Y. Kim, B. H. Kim, and B. I. Min, *Phys. Rev. B* **77**, 035121 (2008).
- ⁴⁵K. Ito, Y. Yasutomi, S. Zhu, M. Nurmatam, M. Tahara, Y. Takeda, Y. Saitoh, K. Toko, R. Akiyama, T. Oguchi, A. Kimura, and T. Suemasu "Manipulation of saturation magnetization and perpendicular magnetic anisotropy in epitaxial $\text{Co}_x\text{Mn}_{4-x}\text{N}$ films with ferrimagnetic compensation" (submitted).
- ⁴⁶E. Goering, S. Gold, and G. Schütz, *J. Synchrotron Rad.* **8**, 422 (2001).
- ⁴⁷H. Maruyama and N. Nakamura, *J. Electron Spectrosc. Relat. Phenom.* **136**, 135 (2004).
- ⁴⁸B. T. Thole, P. Carra, F. Sette, and G. van der Laan, *Phys. Rev. Lett.* **68**, 1943 (1992).

⁴⁹P. Carra, B. T. Thole, M. Altarelli, and X. D. Wang, *Phys. Rev. Lett.* **70**, 694 (1993).

⁵⁰K. Nagai, H. Fujiwara, H. Aratani, S. Fujioka, H. Yomosa, Y. Nakatani, T. Kiss, A. Sekiyama, F. Kuroda, H. Fujii, T. Oguchi, A. Tanaka, J. Miyawaki, Y. Harada, Y. Takeda, Y. Saitoh, S. Suga, and R. Y. Umetsu, *Phys. Rev. B* **97**, 035143 (2018).

⁵¹W. Kuch, J. Gilles, S. S. Kang, S. Imada, S. Suga, and J. Kirschner, *Phys. Rev. B* **62**, 3824 (2000).

⁵²P. Srivastava, N. Haack, H. Wende, R. Chauvistré, and K. Baberschke, *Phys. Rev. B* **56**, R4398 (1997).

⁵³Y. Kong and F. Li, *Phys. Rev. B* **57**, 970 (1998).